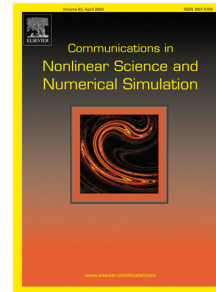


# Journal Pre-proof

An efficient linear and unconditionally stable numerical scheme for the phase field sintering model

Jingjie Cheng, Qing Xia, Junseok Kim, Yibao Li



PII: S1007-5704(23)00450-1

DOI: <https://doi.org/10.1016/j.cnsns.2023.107529>

Reference: CNSNS 107529

To appear in: *Communications in Nonlinear Science and Numerical Simulation*

Received date: 9 June 2023

Revised date: 1 September 2023

Accepted date: 8 September 2023

Please cite this article as: J. Cheng, Q. Xia, J. Kim et al., An efficient linear and unconditionally stable numerical scheme for the phase field sintering model. *Communications in Nonlinear Science and Numerical Simulation* (2023), doi: <https://doi.org/10.1016/j.cnsns.2023.107529>.

This is a PDF file of an article that has undergone enhancements after acceptance, such as the addition of a cover page and metadata, and formatting for readability, but it is not yet the definitive version of record. This version will undergo additional copyediting, typesetting and review before it is published in its final form, but we are providing this version to give early visibility of the article. Please note that, during the production process, errors may be discovered which could affect the content, and all legal disclaimers that apply to the journal pertain.

© 2023 Elsevier B.V. All rights reserved.

**Journal Pre-proof**

<sup>1</sup> An efficient linear and unconditionally stable numerical scheme for the  
<sup>2</sup> phase field sintering model

<sup>3</sup> Jingjie Cheng<sup>a</sup>, Qing Xia<sup>a</sup>, Junseok Kim<sup>b</sup>, Yibao Li<sup>a,\*</sup>

<sup>4</sup> <sup>a</sup>School of Mathematics and Statistics, Xi'an Jiaotong University, Xi'an 710049, China

<sup>5</sup> <sup>b</sup>Department of Mathematics, Korea University, Seoul 02841, Republic of Korea

<sup>6</sup> **Abstract**

In this article, the phase field sintering model, which is composed of a Cahn-Hilliard type equation and several Allen-Cahn type equations, has been considered. On the scalar auxiliary variable framework, we propose a theoretically efficient and stable method for solid-state sintering. In order to overcome the nonlinear issues, we define a stabilized scalar auxiliary variable method and reformulate the phase field sintering model. An efficient and accurate numerical scheme is investigated to solve our model. The scheme consist of several decoupled diffusion equations at every time step. Therefore, our scheme is easy to implement. Then we prove the numerical discrete energy is unconditionally stable. Several numerical simulations in two- and three- dimensional spaces are presented to demonstrate the robustness of our method.

<sup>7</sup> **Keywords:** Phase-field, Scalar auxiliary variable, Solid-state sintering, Unconditional energy stability,  
<sup>8</sup> Second order accuracy

---

<sup>9</sup> **1. Introduction**

<sup>10</sup> Solid-state sintering is one of the most significant technique during the material processing, which turns  
<sup>11</sup> powder into compact body and is widely used in fabricating metal [1], ceramic [2], refractory [3] and ultrahigh  
<sup>12</sup> temperature material [4]. During the sintering process, the particles are bonded to each other, thus sintering  
<sup>13</sup> necks are formed. With the growth of grains and reduction of mainly open porosity, the overall volume of the  
<sup>14</sup> whole system shrink quickly. Terminally the particles become a compact polycrystalline sintered body with  
<sup>15</sup> fully closed porosity. Multiple simultaneous physical processes are involved in sintering as described in [5–  
<sup>16</sup> 10], including different diffusion paths(through surface, grain boundary, and bulk lattice), particle rigid-body  
<sup>17</sup> motions and evaporation-condensation. These mechanisms interact among each other and exert influence  
<sup>18</sup> on the evolution of powder compact microstructure, i.e., shape [5, 11], size [7, 8], relative location [9], and  
<sup>19</sup> crystal orientation of individual grains [10, 12]. The densification and grain growth are two main active

\*Corresponding author

Email addresses: cfdkim@korea.ac.kr (Junseok Kim), yibaoli@xjtu.edu.cn (Yibao Li)

URL: <http://gr.xjtu.edu.cn/web/yibaoli> (Yibao Li)

20 ones competed with each other. Precise control between this two mechanisms is the key point to further  
21 optimize the solid-state sintering technique and expand the industrial applications of sintered materials [27].  
22 However, to prevent melting and re-solidification from the sintering process, the temperature should be set  
23 below the melting point, which guarantees atoms to gain sufficient energy to migrate as well. The overall  
24 thermodynamic energy of the system is then consumed. Hence, extensive investigation on the microstructural  
25 evolution microstructural evolution during sintering process have been performed for the broad industrial  
26 applications.

27 The earliest researches on the microstructural evolution in sintering process is reported by Frenkel [13],  
28 which is considered as the viscous flow phenomenon. Based on their research, Kuczynski [14] reported that  
29 surface diffusion is operative at the beginning of sintering. Subsequent researches [15–22] concluded power  
30 laws to describe sintering progress while few experimental results can fit the theories well. Various numeri-  
31 cal techniques have been developed to study sintering in recent years [23–31]. Zhou et al. [23] developed a  
32 finite-element based model to investigate the viscous sintering of three-dimensional configuration of ternary  
33 particles. The calculations are in good agreement with benchmark results for a two-dimensional axisym-  
34 metric case. Jagota and Dawson [24] carried out a micro mechanical model for the constitutive behavior of  
35 powder compacts for the interaction between particles. In their work, they provided specific experimental  
36 numerical results for linear viscous materials. Zeng et al. [25] employed molecular dynamics methods to  
37 model nanoparticle arrays over a range of temperatures in order to investigate surface energies, grain bound-  
38 ary mobility, and sintering process. Their initial outcomes revealed unexpectedly robust inputs from plastic  
39 deformation, mechanical rotations, amorphization, and ultra-swift atomic force-driven diffusion mechanisms  
40 during the sintering phase of multi-particle arrays. Tikare and Braginsky [26] presented a Monte Carlo  
41 model with kinetic properties, which is able to simulate the sintering process in a two-dimensional system  
42 comprising three particles and track the evolution of the microstructure. The model can simultaneously  
43 simulate multiple mechanisms, and its validity has been established based on changes in morphology and  
44 kinetics of densification. Wang [27] carried out a phase field model of solid-state sintering for multiple  
45 concurrent physical processes. They devised an efficient scheme for translating and rotating particles, using  
46 a grain boundary force formula as the foundation. This type rigid-body motion introduces an advection  
47 term that alters both the Cahn-Hilliard nonlinear diffusion equation and the Ginzburg-Landau equation for  
48 structural relaxation. A numerical method, proposed by Bruchon et al. [29], has been developed to simulate  
49 the transport of mass via surface and lattice diffusion within granular packings. The grains are defined using  
50 Level-Set functions that adhere to physical laws. Comparisons between the numerical results obtained and  
51 those generated by conventional geometric models for two spherical grains are presented. Weiner et al. [28]  
52 used the finite differences method to develop a novel approach for modeling sintering behavior of powder  
53 particles with irregular shapes. They introduced a discrete scheme of irregular powder particles, which is  
54 proved to have better efficiency and the simulation results fit the theories well.

55 Conventional wisdom on solid-state sintering has contributed expensive strategies on the investigation  
56 of microstructural evolution during sintering process. The evolution of solid particles is determined by the  
57 velocity at the surface [29, 32]. This velocity is governed by mass conservation, which is expressed through  
58 flux divergence. The fluxes are supposed to be calculated on moving surfaces or grain boundaries since it  
59 is directly proportional to the negative gradient of the potential energy. Both finite volume method and  
60 finite element method need an indispensable re-meshing process when dealing with sharp-interface problem.  
61 Thus, a huge computational burden is required for constantly re-meshing. However, phase field method,  
62 which is obtained by a sequence of approximations from dynamical density functional theory [33–38], is  
63 an efficient model to solve interfacial problems. This type method employs fixed grid points and traces  
64 the motion of the boundary implicitly with a continuous order parameter. The narrow transition region  
65 defines the position of the mobile interface or boundary, which also advances during the whole sintering  
66 process. The order parameter naturally evolves along the path that minimizes the thermodynamic energy  
67 of the modeled system. Therefore, the phase-field sintering model (PFSM) [27] could be considered as a  
68 Cahn-Hilliard(CH) model [39] that incorporates grain growth [40] on the solid phase [41–43]. Termuhlen  
69 et al. [31] developed a computational scheme to investigate solid-state sintering process, which enables the  
70 direct implementation of an existing formulation for computing the rigid-body movement of grains using  
71 a phase-field sintering model at a large scale. To compute the particle velocity during densification, they  
72 employed a grouping algorithm as well as established a cutoff radius for each grain. Meanwhile, a stabilized  
73 Scalar Auxiliary Variable(SAV) method [47], which is based on the nominal SAV approach [44–46], is used for  
74 solving the phase-field models. Chen et al. [47] developed a ternary CH type Nakazawa-Ohta phase-field  
75 model for the tri-block copolymer, which is a complex and strongly-coupled non-linear system that involves  
76 two CH equations and two non-local equations. To solve the model, they employed a second-order accurate  
77 time-marching scheme constructed using the SAV approach with a stabilization term. The SAV approach is  
78 widely employed as an efficient and accurate temporal discretization scheme for constructing a broad class  
79 of gradient flows. This method introduces auxiliary variables to handle nonlinear terms, allowing it to solve  
80 only a set of decoupled equations with constant coefficients at each time step. Hence, numerous studies  
81 have demonstrated that it enables unconditional energy stability of the numerical scheme [48–50]. The most  
82 notable advantage of this method is its versatility, as it is not limited to specific forms of the nonlinear part  
83 of the free energy, making it applicable to a wide range of gradient flows. As a result, the SAV approach  
84 exhibits higher precision and efficiency compared to existing methods.

85 In this work, we develop a numerical scheme with high efficiency and accuracy to solve the phase field  
86 sintering model. We use the stabilized scalar auxiliary variable method [47] through adding a second-order  
87 linear term. We define a scalar auxiliary variable and rewrite the phase field sintering model in order to  
88 overcome the nonlinear issues. Then we carry out a second-order accurate scheme using the Backward  
89 differentiation formulas(BDF) framework. By defining two inverse linear operators, only several linear

90 biharmonic equations left in the linear system. Then we decouple the system through Picard iteration,  
 91 which guarantees the developed scheme to be highly efficient. The discrete scheme is then proved to preserve  
 92 the unconditional energy stability rigorously. In order to demonstrate the accuracy, the stability and the  
 93 efficiency of the proposed numerical algorithm, we implement various numerical simulations in both two-  
 94 and three-dimensional space.

95 The remaining of the article is orgnized as follows. In Section 2, the governing equations of phase field  
 96 sintering model is developed and the derivation of the energy law is presented rigorously. In Section 3, we  
 97 present the establishment of a temporal semi-discrete scheme which is second-order accuracy, as well as  
 98 its solvability and energy stability. In Section 4, various numerical tests are performed to demonstrate the  
 99 stability and robustness. Finally, we provide some conclusive remarks in Section 5.

100 **2. Governing model**

101 Considering the phase-field sintering model, we use two sets of order parameters to explain the mi-  
 102 crostructure of the entire system. The first-order parameter  $\phi$ , which ranges from 0 (vapor/vacuum) to  
 103 1 (solid), and is used to represent the two distinct components. It is a conserved order parameter since  
 104 changes of the morphology in solid phase are dependent upon mass transport. Meanwhile, the evolution of  
 105  $\phi$  tracks the changes of the solid structure. We use a set of non-conserved order parameters to represent the  
 106 crystal orientations of individual grains in the solid phase. These order parameters are continuous functions  
 107 of both time and space as follows:

$$\eta_1(\mathbf{r}, t), \eta_2(\mathbf{r}, t), \eta_3(\mathbf{r}, t), \dots, \eta_Q(\mathbf{r}, t). \quad (1)$$

108 Each grain is represented by a unique non-conserved order parameter  $\eta_i$  that are a function of time  $t$  and  
 109 position  $\mathbf{r}$ ,  $i = 1, 2, \dots, Q$ , in which the subscript  $i$  indicates the  $i$ -th grain and  $Q$  represents the number of  
 110 grains. Note that both  $\phi$  and  $\eta_i$  belong to the  $L^2$  space, then we define the norms and inner product on the  
 111  $L^2$  space as follows:

$$(\phi, \psi) = \int_{\Omega} \phi \psi d\mathbf{x}, \quad \|\phi\|^2 = (\phi, \phi), \quad \|\nabla \phi\|^2 = (\nabla \phi, \nabla \phi). \quad (2)$$

112 The evolution of the order parameters temporally and spatially is described as follows:

$$\frac{\partial \phi(\mathbf{r}, t)}{\partial t} = M \Delta \frac{\delta F}{\delta \phi(\mathbf{r}, t)}, \quad (3a)$$

$$\frac{\partial \eta_i(\mathbf{r}, t)}{\partial t} = -L \frac{\delta F}{\delta \eta_i(\mathbf{r}, t)}. \quad (3b)$$

113 It can be seen that the two equations above govern the evolution of grain boundaries and free surfaces.  
 114 Equation (3a) takes into account the effect of Ostwald ripening on the entire solid phase, while Eq. (3b)  
 115 accounts for the evolution process of each grain driven by grain growth in the solid phase. It is worth noting  
 116 that in these two equations,  $M$  and  $L$  are positive mobility coefficients, which influence the motion of grain  
 117 boundaries and free surfaces during the evolution process. Meanwhile, these equations can be derived from  
 118 the total free energy  $F$ :

$$F = \int_V \left( f(\phi, \eta_1, \eta_2, \dots, \eta_Q) + \frac{\kappa_\eta}{2} \sum_{i=1}^Q \|\nabla \eta_i\|^2 + \frac{\kappa_\phi}{2} \|\nabla \phi\|^2 \right) dV, \quad (4)$$

119 in which  $\kappa_\eta$  and  $\kappa_\phi$  are positive constants assuming an isotropic gradient energy while  $f$  represents the local  
 120 free energy density with the following formulas

$$f(\phi, \eta_1, \eta_2, \dots, \eta_Q) = A\phi^2(1-\phi)^2 + B \left( \phi^2 + 6(1-\phi) \sum_{i=1}^Q \eta_i^2 - 4(2-\phi) \sum_{i=1}^Q \eta_i^3 + 3 \left( \sum_{i=1}^Q \eta_i^2 \right)^2 \right). \quad (5)$$

121 Here  $A$  and  $B$  are constants, which determine the energy landscape. Thus the governing equations can be  
 122 obtained by using the variational derivation as follows:

$$\frac{\partial \phi(\mathbf{r}, t)}{\partial t} = M \Delta \psi, \quad (6a)$$

$$\psi = 2A\phi(2\phi^2 - 3\phi + 1) + 2B\phi - 6B \sum_{i=1}^Q \eta_i^2 + 4B \sum_{i=1}^Q \eta_i^3 - \kappa_\phi \Delta \phi, \quad (6b)$$

$$\frac{\partial \eta_i(\mathbf{r}, t)}{\partial t} = -L\mu_i, \quad (6c)$$

$$\mu_i = 12B(1-\phi)\eta_i - 12B(2-\phi)\eta_i^2 + 12B\eta_i \sum_{j=1}^Q \eta_j^2 - \kappa_\eta \Delta \eta_i. \quad (6d)$$

123 Alternatively, we can also select a no-flux boundary conditions as follows:

$$\partial_{\mathbf{n}} \eta_i|_{\partial\Omega} = \partial_{\mathbf{n}} \mu_i|_{\partial\Omega} = \partial_{\mathbf{n}} \phi|_{\partial\Omega} = 0, \quad (7)$$

124 where  $\mathbf{n}$  is denoted as the outward normal of  $\partial\Omega$ . Then we propose the following energy dissipation law.

125 **Theorem 1.** The governing system Eqs. (6) preserve the following energy dissipation law:

$$\frac{d}{dt} F(\phi, \eta_1, \eta_2, \dots, \eta_Q) = -L \sum_{i=1}^Q \|\mu_i\|^2 - M \|\nabla \psi\|^2 \leq 0. \quad (8)$$

<sup>126</sup> **Proof.** We take the inner product of Eq. (6c) with  $\mu_i$  and Eq. (6a) with  $\mu$ , which yield that

$$(\eta_{it}, \mu_i) = -L\|\mu_i\|^2, \quad (\phi_t, \psi) = -M\|\nabla\psi\|^2. \quad (9)$$

<sup>127</sup> By summarizing all the obtained equalities, we can get following equation

$$\begin{aligned} & \frac{d}{dt} F(\phi, \eta_1, \eta_2, \dots, \eta_Q) \\ &= \frac{d}{dt} \int_V \left( f(\phi, \eta_1, \eta_2, \dots, \eta_Q) + \frac{\kappa_\eta}{2} \sum_{i=1}^Q \|\nabla \eta_i\|^2 + \frac{\kappa_\phi}{2} \|\nabla \phi\|^2 \right) dV \\ &= \int_V \left( 2A\phi(2\phi^2 - 3\phi + 1)\phi_t + 2B\phi\phi_t - 6B \sum_{i=1}^Q \eta_i^2 \phi_t + 4B \sum_{i=1}^Q \eta_i^3 \phi_t - \kappa_\phi \Delta \phi \phi_t \right) dV \\ &\quad + \sum_{i=1}^Q \int_V \left( 12B(1-\phi)\eta_i \eta_{it} - 12B(2-\phi)\eta_i^2 \eta_{it} + 12B\eta_i \eta_{it} \sum_{j=1}^Q \eta_j^2 - \kappa_\eta \Delta \eta_i \eta_{it} \right) dV \\ &= (\psi, \phi_t) + \sum_{i=1}^Q (\mu_i, \eta_{it}) = -L \sum_{i=1}^Q \|\mu_i\|^2 - M \|\nabla\psi\|^2 \leq 0. \end{aligned} \quad (10)$$

<sup>128</sup> This completes the proof.  $\square$

<sup>129</sup> A new stabilized-SAV approach is then obtained, in which the stabilization term is used to enhance the  
<sup>130</sup> numerical stability, especially when time step reach a large number. We define an auxiliary nonlocal variable  
<sup>131</sup>  $u(t)$  as:

$$u(t) = \sqrt{\int_V f(\phi, \eta_1, \eta_2, \dots, \eta_Q) dV + b}, \quad (11)$$

<sup>132</sup> where  $b$  can chosen as any constant that ensures  $\int_V f(\eta_1, \eta_2, \dots, \eta_Q) dV + b > 0$  for any  $\eta_i$ . We set  $b = 1$  as a  
<sup>133</sup> constant. Substituting Eq. (11) into Eq. (4) and the total energy functional is formulated as follows:

$$F(\phi, \eta_1, \eta_2, \dots, \eta_Q, u) = \int_V \left( \frac{\kappa_\eta}{2} \sum_{i=1}^Q \|\nabla \eta_i\|^2 + \frac{\kappa_\phi}{2} \|\nabla \phi\|^2 \right) dV + u^2 - b. \quad (12)$$

<sup>134</sup> Thus we can rewrite the governing system Eqs. (6) as follows:

$$\phi_t = M\Delta\psi, \quad (13a)$$

$$\psi = -\kappa_\phi \Delta \phi + uH, \quad (13b)$$

$$\eta_{it} = -L\mu_i, \quad (13c)$$

$$\mu_i = -\kappa_\eta \Delta \eta_i + uH_i, \quad (13d)$$

$$u_t = \frac{1}{2} \int_V \left( H\phi_t + \sum_{i=1}^Q H_i \eta_{it} \right) dV, \quad (13e)$$

<sup>135</sup> where

$$\begin{aligned} H &= 2 \frac{\delta u}{\delta \phi} = \frac{2A\phi(2\phi^2 - 3\phi + 1) + 2B\phi - 6B \sum_{i=1}^Q \eta_i^2 + 4B \sum_{i=1}^Q \eta_i^3}{\sqrt{\int_V f(\eta_1, \eta_2, \dots, \eta_Q) dV + b}}, \\ H_i &= 2 \frac{\delta u}{\delta \eta_i} = \frac{12B(1-\phi)\eta_i - 12B(2-\phi)\eta_i^2 + 12B\eta_i \sum_{j=1}^Q \eta_j^2}{\sqrt{\int_V f(\eta_1, \eta_2, \dots, \eta_Q) dV + b}}. \end{aligned} \quad (14)$$

<sup>136</sup> Then we choose the following initial conditions as:

$$\phi(t=0) = \phi^0, \quad \eta_i(t=0) = \eta_i^0, \quad u(t=0) = \sqrt{\int_V f(\phi^0, \eta_1^0, \eta_2^0, \dots, \eta_Q^0) dV + b}. \quad (15)$$

<sup>137</sup> Therefore the new system Eqs. (13) is equivalent to the original system Eqs. (6). We notice that the system  
<sup>138</sup> (13) also follows the energy dissipative law which can be derived as follows. By taking the inner product of  
<sup>139</sup> (13c) with  $\mu_i$  and (13a) with  $\mu$ , we obtain

$$(\eta_{it}, \mu_i) = -L\|\mu_i\|^2, \quad (\phi_t, \psi) = -M\|\nabla\psi\|^2. \quad (16)$$

<sup>140</sup> By summarizing all the obtained equalities, we arrive at

$$\begin{aligned} &\frac{d}{dt} F(\phi, \eta_1, \eta_2, \dots, \eta_Q, u) \\ &= \frac{d}{dt} \int_V \left( \frac{\kappa_\phi}{2} \|\nabla\phi\|^2 + \frac{\kappa_\eta}{2} \sum_{i=1}^Q \|\nabla\eta_i\|^2 \right) dV + \frac{d}{dt} u^2 \\ &= \frac{d}{dt} \int_V \left( \frac{\kappa_\phi}{2} \|\nabla\phi\|^2 + \frac{\kappa_\eta}{2} \sum_{i=1}^Q \|\nabla\eta_i\|^2 \right) dV + u \int_V \left( H\phi_t + \sum_{i=1}^Q H_i \eta_{it} \right) dV \\ &= (\psi, \phi_t) + \sum_{i=1}^Q (\mu_i, \eta_{it}) = -L \sum_{i=1}^Q \|\mu_i\|^2 - M \|\nabla\psi\|^2 \leq 0. \end{aligned} \quad (17)$$

<sup>141</sup> **3. Numerical algorithms**

<sup>142</sup> In this section, we develop a second-order accurate scheme based on the SAV method which is recently  
<sup>143</sup> enhanced by the addition of a linear stabilized term. As a consequence, the stability of the whole system  
<sup>144</sup> gain a significant improvement. Here we discretize the domain  $\Omega = [0, L_x] \times [0, L_y] \in \mathcal{R}^2$  as  $\Omega_d = \{(x_i, y_i) : 1 \leq i \leq Nx, 1 \leq i \leq Ny\}$ . While  $h = L_x/N_x = L_y/N_y$  is defined as the uniform mesh size. Then we define

<sup>146</sup> several discrete operators as follows: The discrete gradient operator is defined as:

$$\nabla_d \phi_{i,j} = \left( D_x \phi_{i+\frac{1}{2},j}, D_y \phi_{i,j+\frac{1}{2}} \right), \quad (18)$$

<sup>147</sup> where  $D_x \phi_{i+\frac{1}{2},j} = (\phi_{i+1,j} - \phi_{i,j})/h$  and  $D_y \phi_{i,j+\frac{1}{2}} = (\phi_{i,j+1} - \phi_{i,j})/h$ . Let us define the discrete Laplacian  
<sup>148</sup> operator as:

$$\Delta_d \phi_{i,j} = \frac{\phi_{i-1,j} + \phi_{i+1,j} + \phi_{i,j-1} + \phi_{i,j+1}}{h^2} \quad (19)$$

<sup>149</sup> Furthermore, some discrete norms and discrete inner products are defined as follows:

$$\|\phi\|_d^2 = (\phi, \phi)_d, \quad \|\nabla_d \phi\|_d^2 = (\nabla_d \phi, \nabla_d \phi)_d, \quad (\phi, \psi)_d = h^2 \sum_{i=1}^{N_x} \sum_{j=1}^{N_y} \phi_{i,j} \psi_{i,j}$$

<sup>150</sup> Now we set a positive integer  $N$  and the time step size  $\delta t$  is defined as  $\delta t = T/N$ . An implicit-explicit  
<sup>151</sup> combination for the nonlinear terms is used along with the second-order finite difference formula derived  
<sup>152</sup> in time in order to construct a numerical scheme for solving the system. As a consequence, Eqs. (13) is  
<sup>153</sup> rewritten as follows:

$$\frac{3\phi^{n+1} - 4\phi^n + \phi^{n-1}}{2M\delta t} = \Delta_d \psi^{n+1}, \quad (20a)$$

$$\psi^{n+1} = -\kappa_\phi \Delta_d \phi^{n+1} + u^{n+1} H^{\star,n+1} + S(\phi^{n+1} - \phi^{\star,n+1}), \quad (20b)$$

$$\frac{3\eta_i^{n+1} - 4\eta_i^n + \eta_i^{n-1}}{2L\delta t} = -\mu_i^{n+1}, \quad (20c)$$

$$\mu_i^{n+1} = -\kappa_\eta \Delta_d \eta_i^{n+1} + u^{n+1} H_i^{\star,n+1} + S(\eta_i^{n+1} - \eta_i^{\star,n+1}), \quad (20d)$$

$$3u^{n+1} - 4u^n + u^{n-1} \quad (20e)$$

$$= \frac{1}{2} \int_V \left( H^{\star,n+1} (3\phi^{n+1} - 4\phi^n + \phi^{n-1}) + \sum_{i=1}^Q H_i^{\star,n+1} (3\eta_i^{n+1} - 4\eta_i^n + \eta_i^{n-1}) \right) dV.$$

<sup>154</sup> Assuming that  $\phi^n, \eta_i^n, u^n$  and  $\phi^{n-1}, \eta_i^{n-1}, u^{n-1}$  are known as:

$$\begin{aligned} \phi^{\star,n+1} &= 2\phi^n - \phi^{n-1}, & H^{\star,n+1} &= H(\phi^{\star,n+1}, \eta_1^{\star,n+1}, \eta_2^{\star,n+1}, \dots, \eta_Q^{\star,n+1}), \\ \eta_i^{\star,n+1} &= 2\eta_i^n - \eta_i^{n-1}, & H_i^{\star,n+1} &= H_i(\phi^{\star,n+1}, \eta_1^{\star,n+1}, \eta_2^{\star,n+1}, \dots, \eta_Q^{\star,n+1}), \end{aligned} \quad (21)$$

<sup>155</sup> where the parameter  $S$  is considered to be a positive stabilization term. Note that we need the values  
<sup>156</sup> of  $\phi^1, \eta_i^1$  and  $u^1$  to calculate the second-order fully-discrete scheme Eqs. (20a)-(20e). In practice, the  
<sup>157</sup> values of these parameters are obtained through using a similar time-marching algorithm which is first-order  
<sup>158</sup> accuracy. Then we discuss the practical implementations of the scheme Eqs. (20a)-(20e). Even it possesses

<sup>159</sup> linear property, the scheme (20a)-(20e) remain difficult to solve as the unknown parameters  $\phi^{n+1}$ ,  $\eta_1^{n+1}$ ,  
<sup>160</sup>  $\eta_2^{n+1} \dots \eta_Q^{n+1}$  and  $u^{n+1}$  are coupled together. In order to deal with this problem, we implement our proposed  
<sup>161</sup> scheme with a decoupling process through Picard iteration shown as follows. The system Eqs.(20a)-(20e) is  
<sup>162</sup> rewritten as follows:

$$\begin{aligned} \frac{3\phi^{n+1}}{2\delta t} + M\kappa_\phi \Delta_d^2 \phi^{n+1} - MS\Delta_d \phi^{n+1} &= \frac{4\phi^n - \phi^{n-1}}{2\delta t} + Mu^{n+1} \Delta_d H^{\star,n+1} - MS\Delta_d \phi^{\star,n+1}, \\ \frac{3\eta_i^{n+1}}{2\delta t} - L\kappa_\eta \Delta_d \eta_i^{n+1} + LS\eta_i^{n+1} &= \frac{4\eta_i^n - \eta_i^{n-1}}{2\delta t} - Lu^{n+1} H_i^{\star,n+1} + LS\eta_i^{\star,n+1}, \quad i = 1, 2, 3, \dots, Q. \end{aligned} \quad (22)$$

<sup>163</sup> Then we define two linear operators:

$$R(\phi) := \left( \frac{3}{2\delta t} + M\kappa_\phi \Delta_d^2 - MS\Delta_d \right) \phi, \quad R_i(\eta_i) := \left( \frac{3}{2\delta t} - L\kappa_\eta \Delta_d + LS \right) \eta_i. \quad (23)$$

<sup>164</sup> With boundary conditions and apply  $R^{-1}(\phi)$  and  $R_i^{-1}(\eta_i)$ , we obtain

$$\phi^{n+1} = R^{-1} \left( \frac{4\phi^n - \phi^{n-1}}{2\delta t} + Mu^{n+1} \Delta_d H^{\star,n+1} - MS\Delta_d \phi^{\star,n+1} \right) := p_\phi^n + u^{n+1} q_\phi^n, \quad (24)$$

$$\eta_i^{n+1} = R_i^{-1} \left( \frac{4\eta_i^n - \eta_i^{n-1}}{2\delta t} - Lu^{n+1} H_i^{\star,n+1} + LS\eta_i^{\star,n+1} \right) := p_{\eta_i}^n + u^{n+1} q_{\eta_i}^n, \quad i = 1, 2, 3, \dots, Q, \quad (25)$$

<sup>165</sup> where

$$\begin{aligned} p_\phi^n &= R^{-1} \left( \frac{4\phi^n - \phi^{n-1}}{2\delta t} - MS\Delta_d \phi^{\star,n+1} \right), \quad q_\phi^n = R^{-1}(M\Delta_d H^{\star,n+1}), \\ p_{\eta_i}^n &= R_i^{-1} \left( \frac{4\eta_i^n - \eta_i^{n-1}}{2\delta t} + LS\eta_i^{\star,n+1} \right), \quad q_{\eta_i}^n = R_i^{-1}(-LH_i^{\star,n+1}), \quad i = 1, 2, \dots, Q. \end{aligned} \quad (26)$$

<sup>166</sup> It indicates that we can update  $p_\phi^n$ ,  $p_{\eta_i}^n$ ,  $q_\phi^n$ ,  $q_{\eta_i}^n$  by solving the following biharmonic equation

$$\left( \frac{3}{2\delta t} + M\kappa_\phi \Delta_d^2 - MS\Delta_d \right) p_\phi^n = \frac{4\phi^n - \phi^{n-1}}{2\delta t} - MS\Delta_d \phi^{\star,n+1}, \quad (27a)$$

$$\left( \frac{3}{2\delta t} - L\kappa_\eta \Delta_d + LS \right) p_{\eta_i}^n = \frac{4\eta_i^n - \eta_i^{n-1}}{2\delta t} + LS\eta_i^{\star,n+1}, \quad (27b)$$

$$\left( \frac{3}{2\delta t} + M\kappa_\phi \Delta_d^2 - MS\Delta_d \right) q_\phi^n = M\Delta_d H^{\star,n+1}, \quad (27c)$$

$$\left( \frac{3}{2\delta t} - L\kappa_\eta \Delta_d + LS \right) q_{\eta_i}^n = -LH_i^{\star,n+1}. \quad (27d)$$

<sup>167</sup> We plug  $\phi^{n+1}$  and  $\eta_i^{n+1}$  into the above equation, the equation for  $u^{n+1}$  is then obtained. Since  $H^{\star,n+1}$  and  
<sup>168</sup>  $H_i^{\star,n+1}$  are both polynomials of degree three for  $\phi$  and  $\eta_i$ , we notice that it is a nonlinear algebraic equation  
<sup>169</sup> for  $u^{n+1}$ , which can be easily solved by using a Picard iteration. That means we can rewrite the equation

170 for  $u^{n+1}$  as

$$\begin{aligned} u^{n,m+1} = & \frac{4}{3}u^n - \frac{1}{3}u^{n-1} + \frac{1}{6}(H^{\star,n+1}, 3(p_\phi^n + u^{n,m}q_\phi^n) - 4\phi^n + \phi^{n-1}) \\ & + \frac{1}{6}\sum_{i=1}^Q(H_i^{\star,n+1}, 3(p_{\eta_i}^n + u^{n,m}q_{\eta_i}^n) - 4\eta_i^n + \eta_i^{n-1}), \end{aligned} \quad (28)$$

171 where we define  $u^{n,0}$  as the known  $u^n$  and the iteration quits only if the stop criterion  $\|u^{n,m+1} - u^{n,m}\|_d \leq$   
 172  $10^{-8}$  is satisfied, when we can consider  $u^{n+1}$  as  $u^{n,m+1}$ .

173 To summarize, the scheme Eqs. (20) can be implemented through following steps:

174 **Step 1**: Compute  $p_\phi^n$ ,  $q_\phi^n$ ,  $p_{\eta_i}^n$  and  $q_{\eta_i}^n$  from Eqs. (27) with finite difference method.

175 **Step 2**: Update  $u^{n+1}$  by solving the Eq. (28) through Picard iteration.

176 **Step 3**: Set  $\phi^{n+1} = p_\phi^n + u^{n+1}q_\phi^n$  and  $\eta_i^{n+1} = p_{\eta_i}^n + u^{n+1}q_{\eta_i}^n$ , then goto the next step.

177 Therefore, from the above practical implementation process, it is easy to notice that the nonlocal term  
 178  $u^{n+1}$  is solved with litter computational cost for each time step. Meanwhile, several linear equations need  
 179 to be solved in our process.

### 180 3.1. Unconditional energy stability for the discrete system

181 Then we drive the unconditional energy stability of the numerical scheme (20) as follows.

182 **Theorem 2.** The time-discrete scheme (20) follows a energy dissipation law as

$$F^{n+1} - F^n \leq -L\delta t \sum_{i=1}^Q \|\mu_i^{n+1}\|_d^2 - M\delta t \|\nabla_d \psi^{n+1}\|_d^2 \leq 0, \quad (29)$$

183 where

$$\begin{aligned} F^{n+1} = & \frac{\kappa_\eta}{2} \sum_{i=1}^Q \frac{\|\nabla_d \eta_i^{n+1}\|_d^2 + \|2\nabla_d \eta_i^{n+1} - \nabla_d \eta_i^n\|_d^2}{2} + \frac{\kappa_\phi}{2} \frac{\|\nabla_d \phi^{n+1}\|_d^2 + \|2\nabla_d \phi^{n+1} - \nabla_d \phi^n\|_d^2}{2} \\ & + \frac{(u^{n+1})^2 + (2u^{n+1} - u^n)^2}{2} + S \sum_{i=1}^Q \frac{\|\eta_i^{n+1} - \eta_i^n\|_d^2}{2} + S \frac{\|\phi^{n+1} - \phi^n\|_d^2}{2}. \end{aligned} \quad (30)$$

184 **Proof.** Let us take the inner product of Eq. (20c) with  $2L\delta t\mu_i^{n+1}$  and Eq. (20a) with  $2M\delta t\psi^{n+1}$  in the  
 185  $L^2$  space, which indicate that

$$\begin{aligned} \left( \frac{3\eta_i^{n+1} - 4\eta_i^n + \eta_i^{n-1}}{2L\delta t}, 2L\delta t\mu_i^{n+1} \right)_d &= -2L\delta t \|\mu_i^{n+1}\|_d^2, \\ \left( \frac{3\phi^{n+1} - 4\phi^n + \phi^{n-1}}{2M\delta t}, 2M\delta t\psi^{n+1} \right)_d &= -2M\delta t \|\nabla_d \psi^{n+1}\|_d^2. \end{aligned} \quad (31)$$

<sup>186</sup> By multiplying (20e) with  $2u^{n+1}$ , we obtain

$$\begin{aligned} & 2u^{n+1}(3u^{n+1} - 4u^n + u^{n-1}) \\ &= u^{n+1} \int_V \left( H^{\star,n+1}(3\phi^{n+1} - 4\phi^n + \phi^{n-1}) + \sum_{i=1}^Q H_i^{\star,n+1}(3\eta_i^{n+1} - 4\eta_i^n + \eta_i^{n-1}) \right) dV. \end{aligned} \quad (32)$$

<sup>187</sup> Let us take the inner product of (20d) with  $3\eta_i^{n+1} - 4\eta_i^n + \eta_i^{n-1}$  as follows:

$$\begin{aligned} & (\mu_i^{n+1}, 3\eta_i^{n+1} - 4\eta_i^n + \eta_i^{n-1})_d \\ &= (-\kappa_\eta \Delta_d \eta_i^{n+1} + u^{n+1} H_i^{\star,n+1} + S(\eta_i^{n+1} - \eta_i^{\star,n+1}), 3\eta_i^{n+1} - 4\eta_i^n + \eta_i^{n-1})_d \\ &= \kappa_\eta (\nabla_d \eta_i^{n+1}, 3\nabla_d \eta_i^{n+1} - 4\nabla_d \eta_i^n + \nabla_d \eta_i^{n-1})_d + u^{n+1} (H_i^{\star,n+1}, 3\eta_i^{n+1} - 4\eta_i^n + \eta_i^{n-1})_d \\ & \quad + S(\eta_i^{n+1} - 2\eta_i^n + \eta_i^{n-1}, 3\eta_i^{n+1} - 4\eta_i^n + \eta_i^{n-1})_d, \end{aligned} \quad (33)$$

<sup>188</sup> and (20b) with  $3\phi^{n+1} - 4\phi^n + \phi^{n-1}$  as follows:

$$\begin{aligned} & (\psi^{n+1}, 3\phi^{n+1} - 4\phi^n + \phi^{n-1})_d \\ &= (-\kappa_\phi \Delta_d \phi^{n+1} + u^{n+1} H^{\star,n+1} + S(\phi^{n+1} - \phi^{\star,n+1}), 3\phi^{n+1} - 4\phi^n + \phi^{n-1})_d \\ &= \kappa_\phi (\nabla_d \phi^{n+1}, 3\nabla_d \phi^{n+1} - 4\nabla_d \phi^n + \nabla_d \phi^{n-1})_d + u^{n+1} (H^{\star,n+1}, 3\phi^{n+1} - 4\phi^n + \phi^{n-1})_d \\ & \quad + S(\phi^{n+1} - 2\phi^n + \phi^{n-1}, 3\phi^{n+1} - 4\phi^n + \phi^{n-1})_d. \end{aligned} \quad (34)$$

<sup>189</sup> By combining Eqs. (31)-(34), we can obtain the follows:

$$\begin{aligned} & F^{n+1} - F^n \\ &= \frac{\kappa_\eta}{2} \sum_{i=1}^Q \left( \frac{\|\nabla_d \eta_i^{n+1}\|_d^2 + \|2\nabla_d \eta_i^{n+1} - \nabla_d \eta_i^n\|_d^2}{2} - \frac{\|\nabla_d \eta_i^n\|_d^2 + \|2\nabla_d \eta_i^n - \nabla_d \eta_i^{n-1}\|_d^2}{2} \right) \\ & \quad + \frac{\kappa_\phi}{2} \left( \frac{\|\nabla_d \phi^{n+1}\|_d^2 + \|2\nabla_d \phi^{n+1} - \nabla_d \phi^n\|_d^2}{2} - \frac{\|\nabla_d \phi^n\|_d^2 + \|2\nabla_d \phi^n - \nabla_d \phi^{n-1}\|_d^2}{2} \right) \\ & \quad + \frac{(u^{n+1})^2 + (2u^{n+1} - u^n)^2}{2} - \frac{(u^n)^2 + (2u^n - u^{n-1})^2}{2} \\ & \quad + S \sum_{i=1}^Q \left( \frac{\|\eta_i^{n+1} - \eta_i^n\|_d^2}{2} - \frac{\|\eta_i^n - \eta_i^{n-1}\|_d^2}{2} \right) + S \left( \frac{\|\phi^{n+1} - \phi^n\|_d^2}{2} - \frac{\|\phi^n - \phi^{n-1}\|_d^2}{2} \right) \\ &= -L\delta t \sum_{i=1}^Q \|\mu_i^{n+1}\|_d^2 - M\delta t \|\nabla_d \psi^{n+1}\|_d^2 \\ & \quad - \frac{\kappa_\eta}{2} \sum_{i=1}^Q \frac{\|\nabla_d \eta_i^{n+1} - 2\nabla_d \eta_i^n + \nabla_d \eta_i^{n-1}\|_d^2}{2} - \frac{\kappa_\phi}{2} \frac{\|\nabla_d \phi^{n+1} - 2\nabla_d \phi^n + \nabla_d \phi^{n-1}\|_d^2}{2} \end{aligned} \quad (35)$$

$$-\frac{(u^{n+1} - 2u^n + u^{n-1})^2}{2} - S \sum_{i=1}^Q \|\eta_i^{n+1} - 2\eta_i^n + \eta_i^{n-1}\|_d^2 - S \|\phi^{n+1} - 2\phi^n + \phi^{n-1}\|_d^2 \leq 0.$$

<sup>190</sup> This completes the proof. □

<sup>191</sup> **Remark 1.** We adopt a second-order energy stable BDF numerical scheme in Eqs. (20), which is still  
<sup>192</sup> rational if we replace the second-order regularization term  $\phi^{n+1} - 2\phi^n + \phi^{n-1}$  with  $dt(\phi^{n+1} - \phi^n)$ . Referring  
<sup>193</sup> to [48–50], the detailed proofs of energy stability with the Crank-Nicolson(CN) scheme have been applied to  
<sup>194</sup> the governing equations within the SAV framework and similar methods are provided. It is easy to conclude  
<sup>195</sup> that applying the CN scheme to Eqs. (13) would yield a similar proof process. This paper focus on the  
<sup>196</sup> establishment of the efficient numerical method on the sintering process, while the comparison between the  
<sup>197</sup> BDF method and CN method is neglected. In the future work, we will consider comparing the computational  
<sup>198</sup> efficiency and the theoretical proof differences between the two methods.

<sup>199</sup> **Remark 2.** It should be noted that we have not included the error estimation and convergence analysis  
<sup>200</sup> in this paper based on the numerical framework. This is due to the fact that the system is formed by a  
<sup>201</sup> combination of a CH equation and several AC-type equations, where the order parametres  $\phi$  and  $\eta_i (i =$   
<sup>202</sup> 1, 2...Q) are intricately coupled. However, there are many existing works that can be referenced, such as  
<sup>203</sup> [51–53], which provided clear and explicit convergence analyses and error estimations for the energy stable  
<sup>204</sup> numerical scheme in a ternary CH system. In [51], detailed proofs for a first-order energy stable scheme in  
<sup>205</sup> the spreading case are carried out specially. The exact solution is subjected to Fourier projection, while the  
<sup>206</sup> initial values are subjected to mass conservation projection. After discretization, an expression for the error  
<sup>207</sup> grid function is obtained. Futhurmore, the convergence analysis is conducted by utilizing straightforward  
<sup>208</sup> Taylor expansions to estimate the truncation error. Similar methods are also mentioned in [54, 55], where  
<sup>209</sup> detailed introductions to Fourier pseudo-spectral method are provided to perform error estimation and  
<sup>210</sup> convergence analysis for second-order schemes under the SAV approach. They accomplished the derivation  
<sup>211</sup> of truncation error estimate from the spectral approximation estimate, thus proving that their schemes  
<sup>212</sup> converges at second-order. Since we adopt a numerical scheme based on the SAV method with an added  
<sup>213</sup> stabilization term, it can be inferred that our scheme also holds second-order accuracy.

#### <sup>214</sup> 4. Numerical simulations

<sup>215</sup> This section contains several numerical simulations in two- and three- dimensional spaces. For example,  
<sup>216</sup> the evolution test of grains, the stability and accuracy test, the comparative test with different initial value  
<sup>217</sup> conditions, and the three dimensional evolution test. The computational domain  $\Omega$  considered in this paper  
<sup>218</sup> is defined as  $[-1, 1] \times [-1, 1]$  which is discretized with a  $256 \times 256$  mesh-grid. Unless otherwise specified, we

choose Neumann boundary conditions for the numerical simulations. Meanwhile, a set of parameter values are used as follows for the numerical simulations:  $S = 1$ ,  $\kappa_\phi = 0.0016$ ,  $\kappa_\eta = 0.0002$ ,  $A = 0.32$ ,  $B = 0.08$ ,  $M = 25$ ,  $L = 10$ . Note that the above parameters are selected without special explanation.

#### 4.1. Evolution test of grains

First, we investigate the evolution of three grains for the proposed algorithm Eqs. (20). The initial conditions are set as follows:

$$\begin{aligned}\eta_i^0 &= \frac{1}{2} - \frac{1}{2} \tanh\left(\frac{\sqrt{(x-x_i)^2 + (y-y_i)^2} - r_i}{\xi_i}\right), i = 1, 2, 3. \\ \phi^0 &= \sum_{i=1}^3 \eta_i^0.\end{aligned}\quad (36)$$

where  $(x_i, y_i)$  represents the location of the grain center, and  $r_i$  is denoted as the radius of grain.

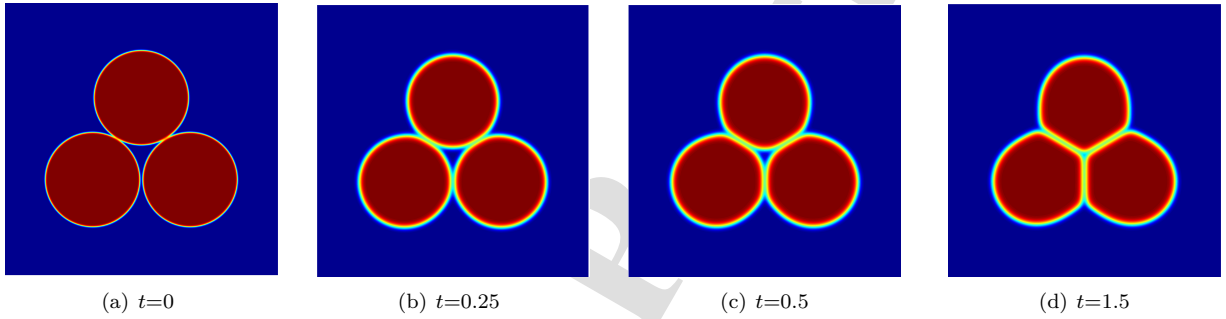
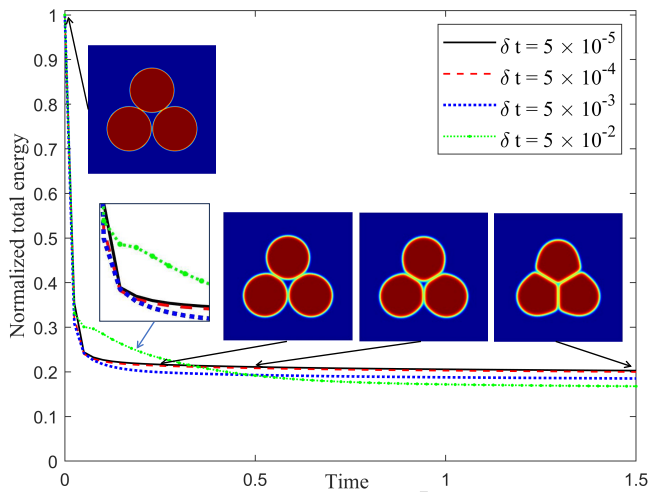


Figure 1: Temporal evolution of a three-grain system in two-dimentional space. The figures represent the morphological evolution of phase field variable  $\phi$  at indicated time points  $t = 0, 0.25, 0.5$  and  $1.5$ , in the  $L_2$  space. And the colour indicates the value of sum of  $\eta_i^2$ .

The procedure is carried out up to  $t = 1.5$  and the time step is chosen as  $\delta t = 5 \times 10^{-5}$ . And we set a relatively small interfacial width as  $\xi = 7.8 \times 10^{-3}$ . The figures above represent the morphological evolution of phase field variable  $\phi$  at specific times  $t = 0, 0.25, 0.5, 1.5$ , respectively. In our tests, we use  $\sum \eta_i^2$  to identify the positions of grain boundaries. The results shown in Fig. 1 demonstrate the evolution of grains during the whole process. Note that the vapor/vacuum phase is indicated by the region colored in blue. At the beginning, the surfaces of voids possess negative curvatures. As particles come into contact, they promptly develop into neck regions, thus creating grain boundaries between adjacent grains. Subsequently, the curvature of small void surfaces changes into a positive value. The first stage of sintering typically refers to the stage where the surfaces of voids possess negative curvature. Once the voids shrink more steadily, the second stage of solid-state sintering begins. With the progress of densification, angles are formed at the points of contact between particles on the solid surfaces, small voids are eliminated at the same time.

237 *4.2. Stability test*

238 In order to demonstrate the stability of the numerical scheme, we conduct a experiment using four  
 239 different time steps,  $\delta t = 5 \times 10^{-5}$ ,  $5 \times 10^{-4}$ ,  $5 \times 10^{-3}$  and  $5 \times 10^{-2}$ , respectively. Then we set the initial  
 240 conditions as Eqs. (36). As shown in Fig. 2, four different time steps are employed to investigate the  
 241 temporal evolution of grains until  $t = 1.5$ . Note that the all four energy curves appear a decreasing trend,  
 242 which means our system follow the energy dissipation law. The figures inserted in Fig. 2 represent the  
 243 evolution of grains with  $\delta t = 5 \times 10^{-3}$  at times 0, 0.25, 0.5 and 1.5, respectively. An enlarged subfigure is  
 244 additionally included in order to clearly demonstrate the differences between curves at the turning points.  
 From the evolution of the grain boundaries, it is easy to notice that our method can be investigated with



245 Figure 2: Temporal evolution of the normalized total energy function using four different time step sizes,  $\delta t = 5 \times 10^{-5}$ ,  
 246  $5 \times 10^{-4}$ ,  $5 \times 10^{-3}$ , and  $5 \times 10^{-2}$  until  $t = 1.5$ , respectively. The figures inserted represent the morphological evolution of phase  
 247 field variable  $\phi$  at indicated time points  $t = 0, 0.25, 0.5$  and  $1.5$ , in the  $L_2$  space, and the colour indicates the value of sum of  
 248  $\eta_i^2$ . Besides, the curves at the corners are also magnified in the subfigures.

249 large time steps. Furthermore, it is obvious that the results with  $\delta t = 5 \times 10^{-5}$  exhibit excellent agreement  
 250 with those obtained by using  $\delta t = 5 \times 10^{-4}$ , but deviate from the outcomes generated by adopting larger  
 251 time steps, such as  $\delta t = 5 \times 10^{-3}$  and  $\delta t = 5 \times 10^{-2}$ . Although the differences are not that significant in  
 252 the large state, a small time step is still suggested to be used in order to achieve more precise numerical  
 solutions. The added stabilized term plays an important role in the process of gradual stabilization. It is  
 obvious that we can easily draw a conclusion that our numerical solution is convergent and the proposed  
 scheme exhibits effectiveness even with large time steps.

253 *4.3. Accuracy test*

254 We investigate the numerical accuracy of the proposed method by evolving the identical initial condition  
 255 over time with finer values for both time intervals and grid spacing. The computational domain is set as

Table 1: Numerical error and convergence rate by using different time steps for the phase field variable  $\phi$  and  $\eta_i$ .

$\delta t$	Error				Order			
	$\phi$	$\eta_1$	$\eta_2$	$\eta_3$	$\phi$	$\eta_1$	$\eta_2$	$\eta_3$
$8.0 \times 10^{-3}$	1.070e-02	3.829e-02	1.697e-02	4.016e-02	—	—	—	—
$4.0 \times 10^{-3}$	2.823e-03	9.244e-03	4.095e-03	9.947e-03	1.92	2.05	2.05	2.01
$2.0 \times 10^{-3}$	6.547e-04	2.180e-03	1.073e-03	2.469e-03	2.11	2.08	1.93	1.90

 Table 2: Numerical error and convergence rate by using different spacial steps for the phase field variable  $\phi$  and  $\eta_i$ .

$N$	Error				Order			
	$\phi$	$\eta_1$	$\eta_2$	$\eta_3$	$\phi$	$\eta_1$	$\eta_2$	$\eta_3$
$128 \times 128$	3.746e-4	1.075e-3	3.763e-4	1.402e-3	—	—	—	—
$256 \times 256$	9.074e-5	2.757e-4	9.920e-5	3.394e-4	2.05	1.96	1.92	2.04
$512 \times 512$	2.348e-5	6.847e-5	2.408e-5	8.858e-5	1.95	2.01	2.04	1.94

[−1, 1] × [−1, 1]. Since there is no closed-form analytical solution exists for our problem, we consider the following reference solution  $\phi^{ref}$ ,  $\eta_1^{ref}$ ,  $\eta_2^{ref}$  and  $\eta_3^{ref}$  as fine values, which are expected to be computed with either a fine time step or a fine grid size. Now we set the initial conditions as follows:

$$\begin{aligned}\eta_i^0 &= \sin(\pi x) \cos(\pi y), i = 1, 2, 3. \\ \phi^0 &= \frac{1}{2}(1 - \sin(\pi x) \cos(\pi x)).\end{aligned}\tag{37}$$

In order to obtain the convergence rates for temporal discretizations, we choose a set of decreasing time steps as  $\delta t = 8 \times 10^{-3}$ ,  $\delta t = 4 \times 10^{-3}$ , and  $\delta t = 2 \times 10^{-3}$  respectively with the fixed spatial size  $h = 1/1024$ . We obtain the fine time step as  $\delta t = 1 \times 10^{-3}$ , thus we gain the expression numerical error as  $e_{i,\delta t} := \phi_{i,\delta t} - \phi_i^{ref}$ . And the definition of the convergence rate in this paper is  $\log_2(||e_{i,\delta t}||_2 / ||e_{i,\delta t/2}||_2)$ . The numerical errors and convergence rates are given in Table 1. As can be seen, our proposed scheme has the second-order temporal accuracy. Then we investigate the spatial convergence rate by using the temporal step size  $\delta t = 1 \times 10^{-4}$ . We employ a set of decreasing spatial steps, namely  $h = 1/128$ ,  $h = 1/256$ ,  $h = 1/512$ , and  $h = 1/1024$ . In addition, the error of a grid is defined as a discrete  $L_2$  norm, i.e.,  $e_{i,h} := \phi_{i,h} - \phi_i^{ref}$ . We also define the convergence rate as the logarithmic ratio of two successive errors, that is,  $\log_2(||e_{i,h}||_2 / ||e_{i,h/2}||_2)$ . The obtained errors and convergence rates using these definitions have been listed in Table 2. The outcomes of our experiments imply that the proposed numerical scheme exhibits second-order accuracy in terms of time.

270

#### 271 4.4. Comparative test on different initial value conditions

We investigate the influence of initial condition on the evolution of grain growth by setting it as a four-grain system, a five-grain system and a six-grain system, respectively. The computational domain is [−1, 1] × [−1, 1]. As shown in Fig. 6, we select four different time points, namely  $t = 0, 0.5, 1$  and  $2.5$ ,

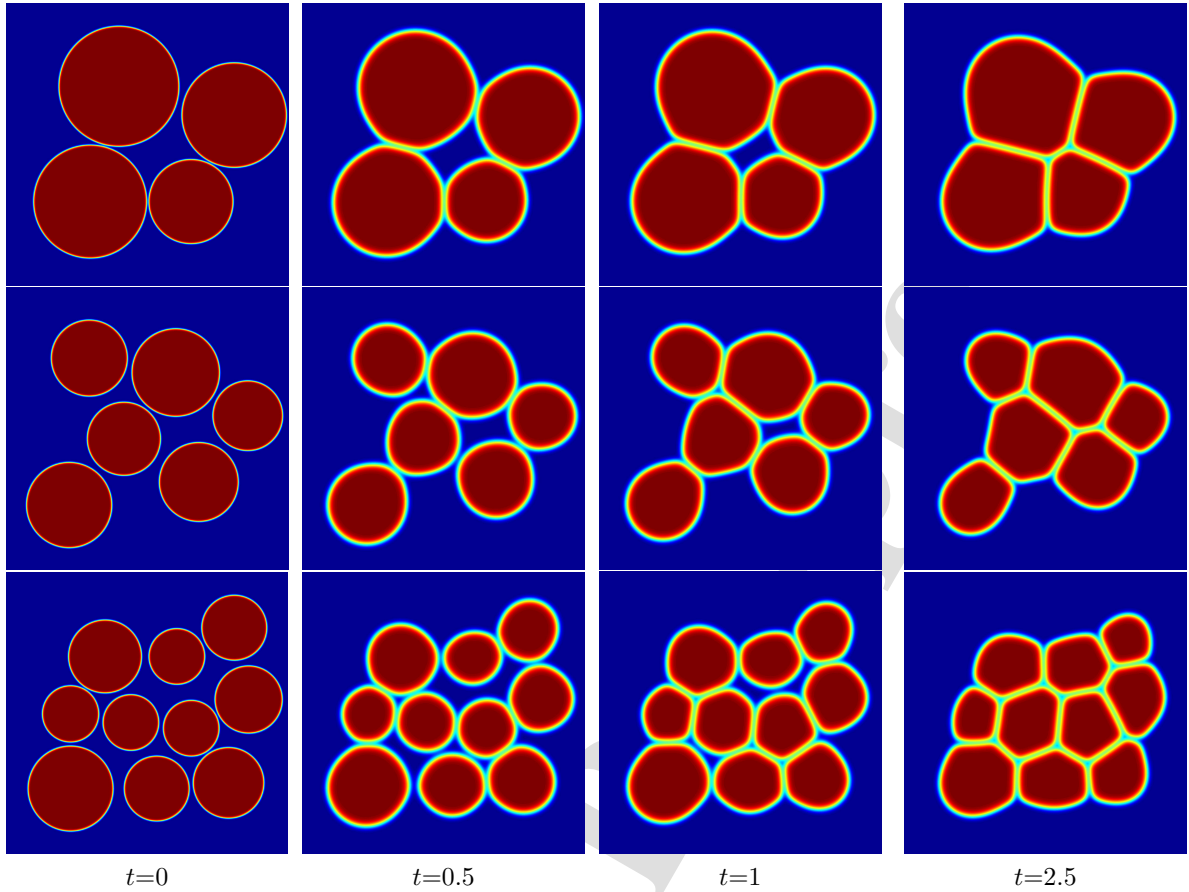


Figure 3: Temporal evolution of multi-grain system in two-dimentional space. The figures represent the morphological evolution of the phase field variable  $\phi$  at indicated time points  $t = 0, 0.5, 1$  and  $2.5$ , respectively. And the colour indicates the value of sum of  $\eta_i^2$ .

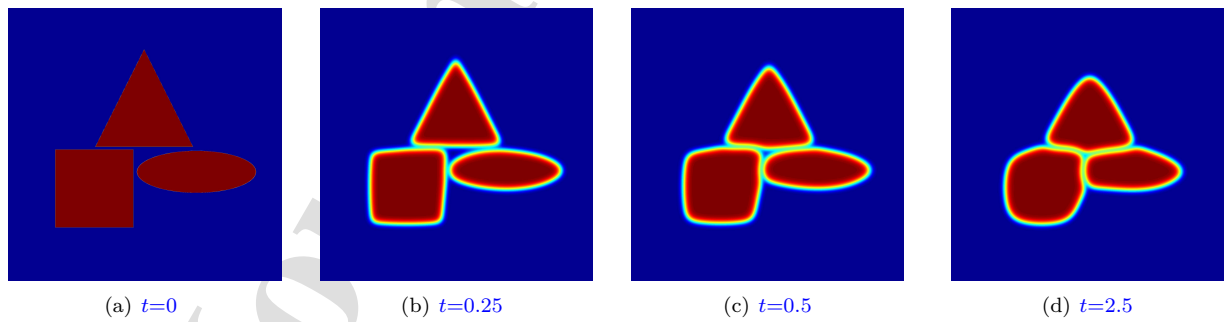


Figure 4: Temporal evolution of a three-grain system in two-dimentional space with square, triangular, and elliptical shapes, respectively. The figures represent the morphological evolution of phase field variable  $\phi$  at indicated time points  $t = 0, 0.25, 0.5$  and  $1.5$ , in the  $L_2$  space. And the colour indicates the value of sum of  $\eta_i^2$ .

275 to analyse the temporal evolution of grain systems using three different initial value conditions. And the  
 276 time step is chosen as  $\delta t = 5 \times 10^{-4}$ . It is obvious that the evolution of grains shows the same tendency as  
 277 three-grain system. We should emphasize that the generation of grain boundaries can not be significantly  
 278 affected by the initial value. As a result, it is obvious that our algorithm works well with any numerous  
 279 grains.

280 Furthermore, we investigate the impact of the initial geometry of grains on the evolution of grain growth.  
 281 As shown in Fig. 4, we select a three-grain systems with square, triangular, and elliptical shapes, respectively.  
 282 The computational domain is denoted as  $[-1, 1] \times [-1, 1]$  and the time interval is set as  $\delta t = 5 \times 10^{-4}$ . Four  
 283 different time points, i.e.,  $t = 0, 0.5, 1$  and  $2.5$  are chosen to illustrate the evolution of our three-grain system  
 284 over time. It is obvious that the initial conditions do not influence the time evolution of the simulation by  
 285 the proposed method.

286 *4.5. Three dimensional test*

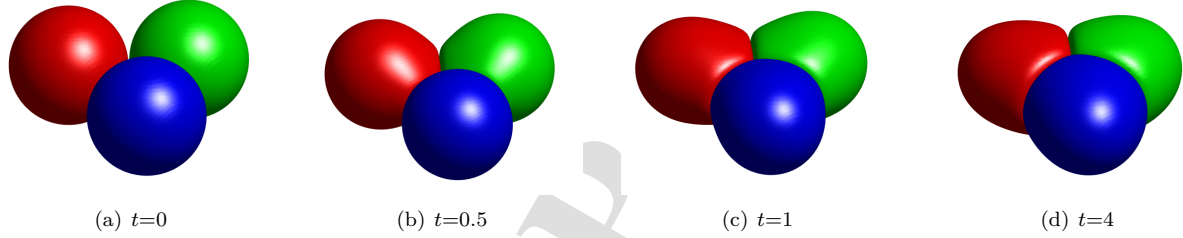


Figure 5: Temporal evolution of the three-grain system of our proposed model in three-dimensional space with  $\delta t = 5 \times 10^{-3}$  until  $t = 4.0$ . The figures represent the morphological evolution of the phase field variable  $\phi$  at indicated time points  $t = 0, 0.5, 1$  and  $4$ , in the  $L_2$  space.

287 As illustrated in Fig. 5, the proposed phase field sintering model is applied in three-dimensional space  
 288 in this subsection. We use a  $128 \times 128 \times 128$  mesh-grid to discretize the computational domain  $\Omega$ , which is  
 289 defined as  $[-1, 1] \times [-1, 1] \times [-1, 1]$ . Then we set the initial conditions as

$$\eta_i^0 = \frac{1}{2} - \frac{1}{2} \tanh\left(\frac{\sqrt{(x-x_i)^2 + (y-y_i)^2 + (z-z_i)^2} - r_i}{\xi_i}\right), i = 1, 2, 3. \quad (38)$$

$$\phi^0 = \sum_{i=1}^3 \eta_i^0. \quad (39)$$

290 where  $(x_i, y_i, z_i)$  represents the location of the grain center, and  $r_i$  is denoted as the radius of grain. Here  
 291 we use a small interface width  $\xi = 1.2 \times 10^{-2}$ . As shown in Fig. 5, we demonstrate the evolution of grain  
 292 boundaries in three-dimensional space at specific times  $t = 0.5, 1, 2$ , and  $4$ , respectively. It is obvious that  
 293 the contacts between particles promptly develop into neck regions, thus creating grain boundaries between  
 294 adjacent grains.

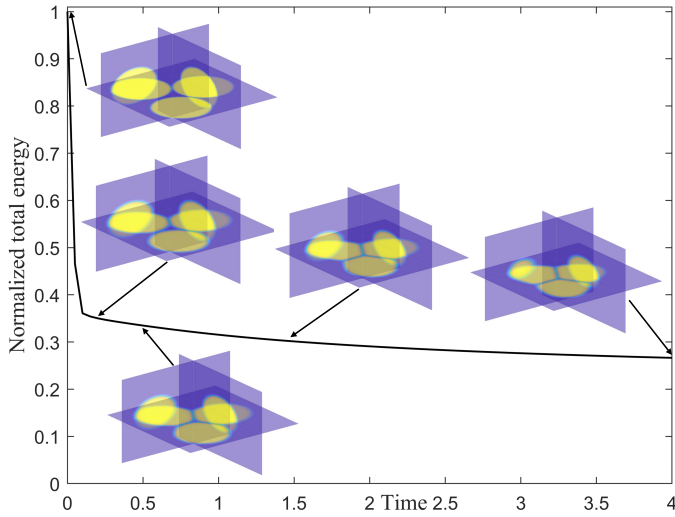


Figure 6: Temporal evolution of the normalized total energy function with time step size of  $\delta t = 5 \times 10^{-3}$  up to  $t = 4$ . The figures inserted represent the slices of morphological evolution of the phase field variable  $\phi$  at specific time points  $t = 0, 0.2, 0.5, 1.5$  and  $4$ , respectively. And the colour indicates the value of sum of  $\eta_i^2$ .

295     The small voids between grains then quickly shrinks, and terminally disappears. Besides, we investigate  
 296     the slices of the morphological evolution of the phase field in three dimension in Fig. 6. The slices are set  
 297     as  $x = 0.25, y = 0.5, z = 0$ , respectively. Compared with the results in two dimension, it is obvious that our  
 298     researches in three dimension is valid.

299     *4.6. Evolution tests on complicated regions*

300     We investigate the evolution of several grains in some complicated regions for the proposed algorithm  
 Eqs. (20), ie, circle and pentagon regions.

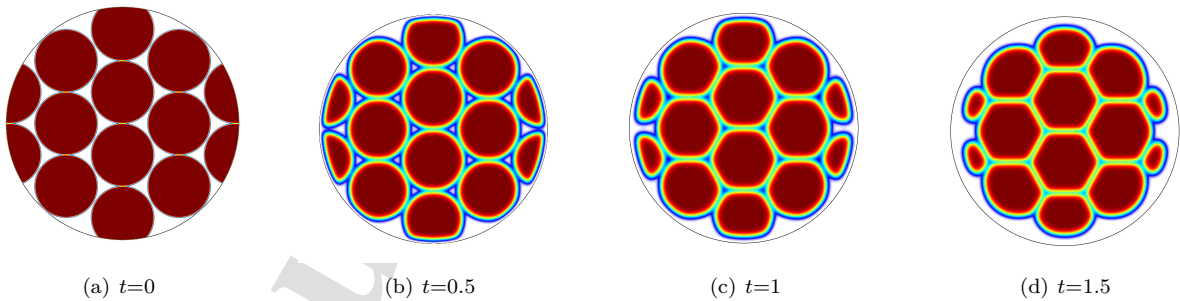


Figure 7: Temporal evolution of multi-grain system in a circle region with  $\delta t = 5 \times 10^{-4}$  until  $t = 1.5$ . The figures represent the morphological evolution of the phase field variable  $\phi$  at indicated time points  $t = 0, 0.5, 1$  and  $1.5$ , in the  $L_2$  space. And the colour indicates the value of sum of  $\eta_i^2$ .

301  
 302     The evolution process in Fig. 7 has been applied until  $t = 1.5$  and the time step is chosen as  $\delta t = 5 \times 10^{-4}$ .  
 303     Here we set a relatively small interfacial width as  $\xi = 7.8 \times 10^{-3}$ . Fig. 7 is the morphological evolution of

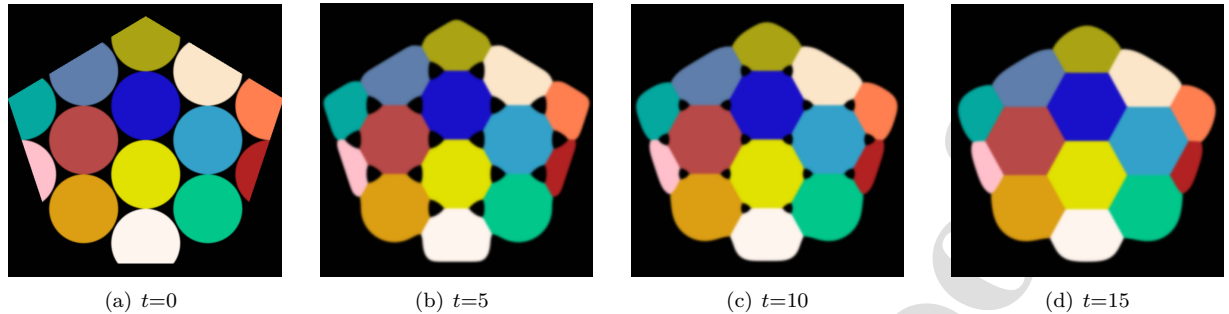


Figure 8: Temporal evolution of the grains of the proposed model with  $\delta t = 5 \times 10^{-4}$  until  $t = 15$ . The figures represent the morphological evolution of the phase field variable  $\phi$  at indicated time points  $t = 0, 5, 10$  and  $15$ , in the  $L_2$  space.

the phase field in a circle region at specific times  $t = 0, 0.5, 1, 1.5$ , respectively. In the above test, we use  $\sum \eta_i^2$  to identify the positions of grain boundaries. The results shown in Fig. 7 indicate that our algorithm is suitable for complicated regions.

In Fig. 8, we colour different grains with different colours to show the morphology evolution of the grains in a pentagon region. In order to better distinguish the grains, we select the parameters as follows:  $\kappa_\phi = 2.2 \times 10^{-5}$  and  $\kappa_\eta = 2 \times 10^{-5}$ . As a result, the evolution procedure is applied until  $t = 15$  with the time step chosen as  $\delta t = 5 \times 10^{-4}$ . And Fig. 8 demonstrate the morphological evolution of the phase field at specific time points  $t = 0, 5, 10, 15$ , respectively.

## 5. Conclusion

The present work presented a phase field sintering model for solid-state sintering and proposed an efficient time marching scheme for the computation. The scheme was rigorously proved to be energy stable. By defining two inverse linear operators, the nonlocal terms are removed and only several linear equations should be solved in the linear system. We presented a rigorous proof for the unconditional energy stability of our numerical scheme. Numerous simulations in two- and three-dimensional spaces were carried out to describe the process of grain growth and demonstrate the efficiency and robustness for our scheme. The numerical results show that our algorithm is equally effective in complex regions and three-dimensional spaces.

### Acknowledgment

Y.B. Li is supported by National Natural Science Foundation of China(No. 12271430).

## References

- [1] X. Lin, M. Huang, H. Zhu, C. Wan, D. Li, L. Jiang, Hydrotalcite-derived nickel–gallium alloy catalysts with enhanced resistance against metal sintering for methane decomposition, Int. J. Hydrogen. Energ., 48 (2023) 10016-10031.

- 326 [2] E. Potanina, L. Golovkina, A. Orlova, A. Nokhrin, M. Boldin, N. Sakharov, Lanthanide (Nd, Gd) compounds with garnet  
327 and monazite structures. Powders synthesis by “wet” chemistry to sintering ceramics by Spark Plasma Sintering, *J. Nucl.*  
328 *Mater.*, 473 (2016) 93-98.
- 329 [3] Z. Grady, A. Ndayishimiye, C. Randal, A dramatic reduction in the sintering temperature of the refractory sodium  
330  $\beta''$ -alumina solid electrolyte via cold sintering, *J. Mater. Chem. A.*, 9 (2021) 22002-22014.
- 331 [4] X. Ren, H. Mo, W. Wang, P. Feng, Li. Guo, Z. Li, Ultrahigh temperature ceramic  $HfB_2 - SiC$  coating by liquid phase  
332 sintering method to protect carbon materials from oxidation, *Mater. Chem. Phys.*, 217 (2018) 504-512.
- 333 [5] S. Kang, *Sintering: Densification, Grain Growth and Microstructure*, Butterworth-Heinemann, Elsevier, 2005.
- 334 [6] M. Barsoum, *Fundamentals of Ceramics*, McGraw-Hill, 1997.
- 335 [7] R. German, *Sintering Theory and Practice*, New York (NY): John Wiley, 1996.
- 336 [8] M. Rahaman, *Ceramic Processing and Sintering*, second ed., CRC Press, 2003.
- 337 [9] Z. Fang, *Sintering of Advanced Materials: Fundamentals and Processes*, Woodhead Publishing Limited, 2010.
- 338 [10] R. German, *Sintering from Empirical Observations to Scientific Principles*, Butterworth-Heinemann, Elsevier, 2014.
- 339 [11] Q. Xia, G. Sun, J. Kim, Y. Li, Multi-scale modeling and simulation of additive manufacturing based on fused deposition  
340 technique, *Phys. Fluids.*, 35 (2023) 034116.
- 341 [12] Y. Li, K. Qin, Q. Xia, J. Kim, A second-order unconditionally stable method for the anisotropic dendritic crystal growth  
342 model with an orientation-field, *Appl. Numer. Math.*, 184 (2023) 512-526.
- 343 [13] J. Frenkel, Viscous flow of crystalline bodies under the action of surface tension, *J. Phys. I.*, 9 (1945) 385-391.
- 344 [14] G. Kuczynski, Self-diffusion in sintering of metallic particles, *Trans. AIME*, 85 (1949) 169-178.
- 345 [15] W. Kingery, M. Berg, Study of the initial stages of sintering solids by viscous flow, evaporation-condensation, and self-  
346 diffusion, *J. Appl. Phys.*, 26 (1955) 1205.
- 347 [16] R. Coble, Sintering crystalline solids. II. experimental test of diffusion models in powder compacts, *J. Appl. Phys.*, 32  
348 (1961) 793
- 349 [17] D. Johnson, I. Cutler, Diffusion sintering: I, Initial state sintering models and their application to shrinkage of powder  
350 compacts, *J. Am. Ceram. Soc.*, 46 (1963) 541.
- 351 [18] D. Johnson, T. Clarke, Grain boundary and volume diffusion in the sintering of silver, *Acta. Metall.*, 12 (1964) 1173-1179.
- 352 [19] R. Coble, Initial sintering of alumina and hematite, *J. Am. Ceram. Soc.*, 41 (1958) 55.
- 353 [20] F. Nichols, W. Mullins, Morphology changes of a surface of revolution due to capillarity-induced surface diffusion, *J. Appl.*  
354 *Phys.*, 36 (1965) 1826.
- 355 [21] D. Johnson, New method of obtaining volume, grain-boundary, and surface diffusion coefficients from sintering data, *J.*  
356 *Appl. Phys.*, 40 (1969) 192-200.
- 357 [22] H. Exner, Principles of single phase sintering, *Rev. Powder. Metall. Phys. Ceram.*, 1 (1979) 7.
- 358 [23] H. Zhou, J. Derby, Three-dimensional finite-element analysis of viscous sintering, *J. Am. Ceram. Soc.*, 81 (1998) 533-540.
- 359 [24] A. Jagota, P. Dawson, Micromechanical modeling of powder compacts: I, Unit problems for sintering and traction induce  
360 deformation, *Acta. Metall.*, 36 (1998) 2551-2561.
- 361 [25] P. Zeng, S. Zajac, P. Clapp, J. Rifkin, Nanoparticle sintering simulations, *Mater. Sci. Eng. A.*, 252 (1998) 301-306.
- 362 [26] V. Tikare, M. Braginsky, Numerical simulation of solid-state sintering: I, Sintering of three particles, *J. Am. Ceram. Soc.*,  
363 86 (2003) 49-53.
- 364 [27] Y. Wang, Computer modeling and simulation of solid-state sintering: A phase field approach, *Acta. Metall.*, 54 (2006)  
365 953-961.
- 366 [28] M. Weiner, M. Schmidtchen, U. Prahl, A new approach for sintering simulation of irregularly shaped powder particles—  
367 Part I: Model development and case studie, *Adv. Eng. Mater.*, 24 (2022) 1438-1656.
- 368 [29] J. Bruchon, D. Mun, F. Valdivieso, S. Drapier, Finite element simulation of mass transport during sintering of a granular

- packing. Part I. Surface and lattice diffusions, *J. Am. Ceram. Soc.*, 95 (2012) 2398–2405.
- [30] M. Weiner, T. Zienert, M. Schmidtchen, J. Hubálková, C. Aneziris, U. Prahl, A new approach for sintering simulation of irregularly shaped powder particles— Part II: Statistical powder modeling, *Adv. Eng. Mater.*, 24 (2022) 2200443.
- [31] R. Termuhlena, X. Chatzistavroub, J. Nicholasb, H. Yua, Three-dimensional phase field sintering simulations accounting for the rigid-body motion of individual grains, *Comp. Mater. Sci.*, 186 (2021) 109963.
- [32] D. Muñoz, J. Bruchon, S. Drapier, F. Valdivieso, High performance computing of sintering process at particle scale, Second ECCOMAS Young Investigators Conference, Bordeaux, France, 2013.
- [33] Q. Xia, Y. Liu, J. Kim, Y. Li, Binary thermal fluids computation over arbitrary surfaces with second-order accuracy and unconditional energy stability based on phase-field model, *J. Comput. Appl. Math.*, 433 (2023) 115319.
- [34] D. Ma, G. Xia, L. Zong, Y. Jia, Y. Tang , R. Zhi, Experimental investigation of flow boiling heat transfer performance in zigzag microchannel heat sink for electronic cooling devices, *Int. J. Therm. Sci.*, 145 (2019) 106003.
- [35] Q. Xia, J. Yang, Y. Li, On the conservative phase-field method with the N-component incompressible flows, *Phys. Fluids.*, 35 (2023) 012120.
- [36] Q. Xia, G. Sun, Q. Yu, K. Junseok, Y. Li, Thermal-fluid topology optimization with unconditional energy stability and second-order accuracy via phase-field model, *Commun. Nonlinear. Sci.*, 116 (2023) 106782.
- [37] Q. Xia, K. Junseok, B. Xia, Y. Li, An unconditionally energy stable method for binary incompressible heat conductive fluids based on the phase–field model, *Comput. Math. Appl.*, 123 (2022) 26-39.
- [38] Q. Xia, X. Jiang, Y. Li, A modified and efficient phase field model for the biological transport network, *J. Comput. Phys.*, 488 (2023) 112192.
- [39] J. Cahn, J. Hilliard, Free energy of a nonuniform system. I. Interfacial free energy, *J. Chem. Phys.*, 28 (1958) 258-267.
- [40] D. Fan, L. Chen, Computer simulation of grain growth using a continuum field model, *Acta. Metall.*, 45 (1997) 611-622.
- [41] Y. Wang, Y. Liu, C. Ciobanu, B. Patton, Simulating microstructural evolution and electrical transport in ceramic gas sensors, *J. Am. Ceram. Soc.*, 83 (2000) 2219-2226.
- [42] K. Ahmed, C. Yablinsky, A. Schulte, T. Allen, A. El-Azab, Phase field modeling of the effect of porosity on grain growth kinetics in polycrystalline ceramics, *Modelling. Simul. Mater. Sci. Eng.*, 21 (2013) 492-508.
- [43] K. Ahmed, T. Allen, A. El-Azab, Phase field modeling for grain growth in porous solids, *J. Mater. Sci.*, 51 (2016) 1261-1277.
- [44] C. Chen , X. Yang , Efficient numerical scheme for a dendritic solidification phase field model with melt convection, *J. Comput. Phys.*, 388 (2019) 41-62 .
- [45] C. Chen , X. Yang , Fast, provably unconditionally energy stable, and second-order accurate algorithms for the anisotropic Cahn-Hilliard Model, *Compute. Method. Appl. M.*, 351 (2019) 35-59.
- [46] Q. Cheng , J. Shen , Multiple scalar auxiliary variable (MSAV) approach and its application to the phase-field vesicle membrane model, *SIAM. J. Sci. Comput.*, 40 (2018) A3982-A4006.
- [47] C. Chen, X. Li, J. Zhang, X. Yang, Efficient linear, decoupled, and unconditionally stable scheme for a ternary Cahn-Hilliard type Nakazawa-Ohta phase-field model for tri-block copolymers, *Appl. Math. Comput.*, 388 (2021) 125463.
- [48] Q. Cheng, C. Liu, J. Shen, A new Lagrange multiplier approach for gradient flows, *Comput. Methods. Appl. Mech. Engrg.*, 367 (2020) 113070.
- [49] J. Shen, J. Xu, J. Yang, The Scalar Auxiliary Variable(SAV) approach for gradient flows, *J. Comput. Phys.*, 353 (2018) 407–416.
- [50] J. Shen, J. Xu, J. Yang, A new class of efficient and robust energy stable schemes for gradient flows, *SIAM Rev.*, 61 (3) (2019) 474–506.
- [51] W. Chen, C. Wang, S. Wang, X. Wang, S. M. Wise, Energy stable numerical schemes for ternary Cahn-Hilliard system, *J. Sci. Comput.*, 84 (2020) 27.
- [52] M. Yuan, W. Chen, C. Wang, S. M. Wise, Z. Zhang, An energy stable finite element scheme for the three-component

- 412 Cahn–Hilliard-Type model for macromolecular microsphere composite hydrogels, J. Sci. Comput., 87 (2021) 78.
- 413 [53] L. Dong, C. Wang, S. M. Wise, Z. Zhang, A positivity-preserving, energy stable scheme for a ternary Cahn–Hilliard system  
414 with the singular interfacial parameters, J. Comput. Phys., 422 (2021) 110451.
- 415 [54] M. Wang, Q. Huang, C. Wang, A second order accurate scalar auxiliary variable (SAV) numerical method for the square  
416 phase field crystal equation, J. Sci. Comput., 88 (2021) 33.
- 417 [55] Q. Cheng, C. Wang, Error estimate of a second order accurate scalar auxiliary variable (SAV) numerical method for the  
418 epitaxial thin film equation, Adv. Appl. Math. Mech., 13 (2021) 1318-1354.

## Highlights

- An unconditional energy stable scheme is proposed for the phase field based sintering model.
- Our proposed scheme has second-order temporal and spatial accuracy.
- Various qualitative and quantitative tests are performed to demonstrate the superiority and robustness of our method.

## Author Statement

**Jingjie Cheng:** Conceptualization; Methodology; Software; Investigation; Visualization; Writing

- Original Draft

**Qing Xia:** Conceptualization; Writing - Review & Editing; Methodology;

**Junseok Kim:** Supervision; Methodology;

**Yibao Li:** Conceptualization; Methodology; Software; Writing - Review & Editing; Supervision;

Project Administration

**Declaration of interests**

The authors declare that they have no known competing financial interests or personal relationships that could have appeared to influence the work reported in this paper.

The authors declare the following financial interests/personal relationships which may be considered as potential competing interests: